Research Article

Maximilian Wolz*, Thomas Kupfer, Horst Drechsel, Ulrich Heber, Andreas Irrgang, J.J. Hermes, Steven Bloemen, David Levitan, Vik Dhillon, and Tom R. Marsh

Spectroscopic and photometric analysis of the HW Vir star PTF1 J011339.09+225739.1

https://doi.org/10.1515/astro-2018-0011
Received Oct 10, 2017; accepted Dec 08, 2017

Abstract: HW Vir systems are rare eclipsing binary systems including a subdwarf B star (sdB) with a faint companion, mostly M-dwarfs. Up to now, 19 HW Vir systems have been published, three of them with substellar companions. We report the spectroscopic as well as photometric observation of the eclipsing sdB binary PTF1 J011339.09+225739.1 (PTF1 J0113) in a close (a=0.722 ± 0.023 $R_\odot$), short period (P = 0.0933731(3)d) orbit. A quantitative spectral analysis of the sdB yields $T_{\rm eff}$=29280 ± 720 K, log(g)=5.77 ± 0.09 dex, and log(y)=−2.32 ± 0.12. The circular orbital velocity of the sdB of K_1=74.2 ± 1.7 km s^{-1} is derived from the radial velocity curve. Except for the strong reflection effect, no other light contribution of the companion could be detected. The light curves - recorded with ULTRACAM - were analyzed using the Wilson-Devinney code. We find an inclination angle of i=79.88 ± 0.18°. Because our first attempts to determine q failed, we calculated large grids of synthetic lightcurves for several mass ratios. Because of degeneracy, good solutions for different mass ratios were found - the one at q = 0.24 is consistent with the sdB's canonical mass ($M_{\rm sdB}$ = 0.47 $M_\odot$). Accordingly, the mass of the companion is M_2=0.112 ± 0.003 $M_\odot$. The radii of the two components were also derived: $R_{\rm sdB}$=0.178 ± 0.006 $R_\odot$ and R_2 = 0.158 ± 0.009 $R_\odot$. Thus, the results for the secondary are consistent with an M-dwarf as secondary.

Keywords: subdwarfs, binaries: eclipsing, stars: early-type, stars: evolution, stars: fundamental parameters, stars: horizontal-branch

1 Introduction

Hot subdwarfs (sdOs, sdBs) are core helium-burning stars with masses around 0.5 $M_\odot$ and very thin hydrogen envelopes that are located at the blue end of the horizontal branch (see Heber, 2009, 2016, for reviews). They can be found in all Galactic stellar populations and are a possible explanation for the UV-upturn of early-type galaxies (Brown et al., 1997). In order to form such an object, the progenitor star has to lose almost its entire hydrogen envelope during the red-giant phase. Even though, the exact evolutionary tracks are unknown today, binary inter-

Corresponding Author: Maximilian Wolz: Dr. Karl Remeis-Observatory & ECAP, Astronomical Institute, Friedrich-Alexander-University of Erlangen-Nuremberg, Sternwartstr. 7, 96049 Bamberg, Germany; Email: max.wolz@fau.de
Thomas Kupfer: Division of Physics, Mathematics, and Astronomy, California Institute of Technology, Passadena, CA 91125, United States of America; Email: tkupfer@caltech.edu
Horst Drechsel: Dr. Karl Remeis-Observatory & ECAP, Astronomical Institute, Friedrich-Alexander-University of Erlangen-Nuremberg, Sternwartstr. 7, 96049 Bamberg, Germany; Email: horst.drechsel@sternwarte.uni-erlangen.de
Ulrich Heber: Dr. Karl Remeis-Observatory & ECAP, Astronomical Institute, Friedrich-Alexander-University of Erlangen-Nuremberg, Sternwartstr. 7, 96049 Bamberg, Germany; Email: ulrich.heber@sternwarte.uni-erlangen.de
Andreas Irrgang: Dr. Karl Remeis-Observatory & ECAP, Astronomical Institute, Friedrich-Alexander-University of Erlangen-Nuremberg, Sternwartstr. 7, 96049 Bamberg, Germany; Email: andreas.irrgang@fau.de
J.J. Hermes: Department of Physics and Astronomy, University of North Carolina, Chapel Hill, NC 27599, United States of America; Email: jjhermes@unc.edu
Steven Bloemen: Department of Astrophysics/IMAPP, Radboud University Nijmegen, P.O. Box 9010, NL-6500 GL Nijmegen, Netherlands; Email: s.bloemen@astro.ru.nl
David Levitan: Division of Physics, Mathematics and Astronomy, California Institute of Technology, Pasadena, CA 91125, United States of America
Vik Dhillon: Department of Physics & Astronomy, University of Sheffield, Sheffield, S3 7RH, United Kingdom; Instituto de Astrofísica de Canarias (IAC), E-38200 La Laguna, Tenerife, Spain
Tom R. Marsh: Department of Physics, University of Warwick, Coventry CV4 7AL, United Kingdom; Division of Physics, Mathematics and Astronomy, California Institute of Technology, Pasadena, CA 91125, United States of America

actions seems to play an important role for the emergence of sdBs because a large proportion of hot subdwarfs (40 to 80 %) is in close binary systems (Maxted et al., 2001; Napiwotzki et al., 2004). Han et al. (2002, 2003) and Podsiadlowski et al. (2008) proposed several binary formation channels for sdB stars:

a) The first is called the “common envelope ejection channel“ (CEE channel). In this scenario, two main sequence (MS) stars evolve in a binary in which the more massive primary star reaches the red giant branch (RGB) first. Near the top of the RGB, the primary fills its Roche lobe and mass transfer occurs. The mass transfer rate is so high that a common envelope (CE) is formed. Because of friction with the envelope, the two cores lose orbital energy and spiral towards each other. If the released orbital energy is high enough, the envelope can be ejected ending the spiral-in phase and a very close binary system remains. Depending on, whether one or two Roche lobe overflows (RLOFs) occur, the post common envelope (PCE) binary consists of a sdB and a late main sequence star - such as the HW Vir systems - or it comprises a sdB and a white dwarf (WD). All sdB stars, that evolved from low mass stars and result from the CEE channel, should have masses just above the critical core mass for the helium flash. Their mass distribution peaks near the canonical mass (0.47 $M_{\odot}$).
b) The second scenario is the "stable Roche lobe overflow channel. As seen before, again, the primary fills its Roche lobe near the RGB tip. The main difference to the CEE channel is that the mass transfer is stable and, hence, does not provoke a CE nor does it lead to a spiral-in phase. Rather, the red giant loses most of its envelope by the Roche lobe overflow. After the hydrogen envelope has been almost completely transferred, the mass transfer stops and a binary system comprising a sdB star with a MS companion remains. SdB binary systems, which passed the stable RLOF, are predicted to have periods between 10 and 1000 days.

Several studies examined the orbital parameters of short-period sdB binaries (e.g. Morales-Rueda et al., 2003, or Edelmann et al., 2005) with the result that the found periods range between 0.05 and more than 10 days with a peak around 0.5 and 1.0 days. Hence, for these close binary sdBs, common envelope ejection (CEE) is the only viable formation channel.

For almost 40 years it has been known that close binaries, which consist of a sdB and a late MS star, do exist (Kilkenny et al., 1978). Getting information about the companion’s parameters from spectroscopy and photometry is not easy, because the companion is so faint. The radial velocity curve of the sdB and the reflection effect - caused by the heated hemisphere of the companion - are the best tools to investigate the parameters of the secondary. Single-lined sdO/B+dM binaries, that do show eclipses as well as reflection effects, are called HW Vir systems. Most of them have short periods ($\sim$ 0.1 d) and a late M-dwarf as companion, but also systems with brown dwarfs as secondary were described (e.g. Geier et al., 2011). Currently, only nineteen HW Vir systems are known (see Schindewolf et al., 2015; Schaffenroth et al., 2014a,b). HW Vir systems are quite important as they offer the opportunity to measure all stellar parameters of the systems. The analysis of the spectra yields the radial velocity (RV) curve and the atmospheric parameters of the sdB. The light curve analysis gives the inclination i.a. and the mass ratio q of the system and by means of the canonical mass, that remains valid for HW Vir systems (Han et al., 2003), we can derive the mass of the companion.

In this paper, we report a new HW Vir system discovered with the Palomar Transient Factory (PTF) program and present the observations as well as the spectroscopic and photometric analysis of this binary which was previously being handled as a white dwarf candidate. Kao et al. (2016) analyzed this system as part of a larger sample. In this connection, PTF1 J011339.09+225739.1 (shortcut: PTF1 J0113) turned out to be a binary consisting of a sdB and an M-dwarf with a magnitude of $R = 16.98 \pm 0.56$ mag.

PTF was a fully-automated, wide-field survey using a 8.1 square degree camera mounted on a 1.2 m telescope at the Palomar Observatory for a systematic exploration of the optical transient sky (Law et al., 2009). In 2012, a follow-up project, called intermediate PTF or iPTF, started using a higher-resolution camera.

At first, we describe the spectroscopic and photometric observations (see Sect. 2), then their analysis in Sect. 3 (spectroscopy) and Sect. 4 (photometry). Finally, we summarize and discuss our results in Sect. 5.

2 Observations

2.1 Spectroscopy

In total, 43 spectra of PTF1 J011339.09+225739.1 (shortcut: PTF1 J0113) were taken, of which 21 were recorded at the Palomar 200-inch telescope (P200) with the Double Spectrograph (DBSP) using a low resolution $R \approx 1500$ (Oke &

Gunn, 1982) and 22 spectra at the Keck II 10m-telescope with the Echellete Spectrograph and Imager (ESI) that offers a higher resolution $R \approx 8000$ (Sheinis et al., 2002). All spectra exhibit strong Balmer lines, that are broadened by the Stark effect, as well as weak helium lines.

We started our analysis by investigating the DBSP spectra: The DBSP is using a dichroic to split the light into a blue and a red channel. The wavelength ranges are $\lambda = 3800-5700$ Å for the blue and $\lambda = 5500-10000$ Å for the red parts. To prevent orbital smearing, the exposure time was set to 180 and 300s respectively for each spectrum. Furthermore, a blaze grating with 600 lines/4000 mm at an angle of 27°17" was chosen. The observations took place on Dec. 23, 2014 and Jan. 24, 2015. Because radial velocities derived from the blue and the red channel were discrepant, we also rereduced the raw spectra as described in Sect. 3. Original DBSP spectra were reduced using the Starlink packages kappa, figaro, and convert for the reduction and calibration (Currie et al., 2014) and the Pamela Code (Marsh, 1989) for the data extraction.

Additionally, we analyzed 22 Keck spectra taken with the ESI spectrograph, operated in the Echellete mode. The exposure time was set to 360 s, the wavelength range covered $\lambda = 3950 - 10500$ Å, and the observation took place on Jul. 8, 2016. The ESI data were reduced with the pipeline Makee.[1]

2.2 Photometry

To conduct the photometric analysis, we used a light curve that was recorded with the ULTRA fast CAMera (ULTRACAM) at the 4.2 m William-Herschel telescope (WHT) on La Palma. ULTRACAM is a transportable, high-speed 3-channel-imager (Dhillon et al., 2007). For the observation of PTF1 J0113, that took place on Sep. 21, 2015, bandpass-filters in the blue, green, and red (u'-, g'-, and r'-channel) were used. The photometric observations were reduced using the ULTRACAM reduction pipeline[2] and then flux calibrated.

3 Spectroscopic analysis

For the following analysis, we used the Spectrum Plotting and Analysis Suite (SPAS, Hirsch 2009). SPAS is based on a χ^2-minimization procedure described by Napiwotzki (1999) using the downhill simplex algorithm.

3.1 Radial velocity curve

Initially, we utilized the spectra prereduced at Palomar. Since the system is classified as a HW Vir type, the spectra are single-lined and the radial velocity can easily be measured by fitting a combination of Gaussian, Lorenzian, and polynomial functions to the absorption lines in the blue and red part of the spectrum, respectively. Because the wavelength interval for the red part is 5500 – 10000 Å, only the H_α line could be used, while in the blue the Balmer hydrogen lines H_β – $H9$ as well as the weak He I 4471 Å line are available. In the blue part of each spectrum, all given lines were fitted simultaneously by the χ^2-minimization and the wavelength shifts with respect to the rest wavelengths are measured. Subsequently, the radial velocities and their related 1σ-uncertainties were calculated from Doppler formula.

Because the orbital period is short, the orbit should be circular. For this reason, we assumed the eccentricity of the system e to be zero so that the radial velocity curve (RV curve) is sinusoidal. Hence, we fitted a sine curve to the RVs derived from the blue part of the spectra and another to the RVs that we had measured for H_α in the red channel. Figure 1 illustrates the best-fit solutions for the blue (left) as well as for the red part (right) of the recorded spectra. We derived semiamplitudes of $K_{1,\mathrm{blue}}$=95 ± 4 km s^{-1} in the blue and $K_{1,\mathrm{red}}$=46 ± 7 km s^{-1} in the red so that the semi-amplitude for the blue part of the spectra would be twice as large as for the red. Also, the reduced χ^2 are quite poor - χ^2_{red}=1.72 and χ^2_{blue}=2.10, respectively.

A detailed analysis of these deviations between the blue and the red brought multiple conspicuities to light:

- When we compared the measured radial velocities of the blue and the red channel for each spectrum, we found large shifts varying widely up to 200 km s^{-1}.
- The most important problem is the fact that just four calibration spectra per night have been recorded (two at the beginning and another two at the end of each observation night). We suspect that flexure of the spectrograph mainly causes the calibration

1 http://www.astro.caltech.edu/~tb/ipac_staff/tab/makee/

2 For further and really detailed information have a look at the ULTRACAM pipeline software web page: http://deneb.astro.warwick.ac.uk/phsaap/software/ultracam/html/index.html

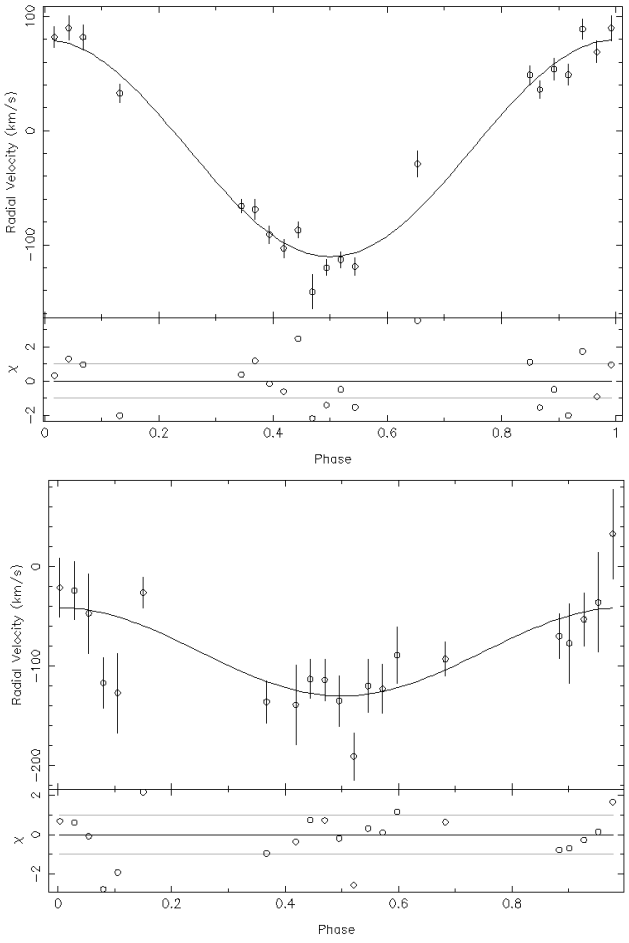

Figure 1. RV of PTF1 J0113 plotted against its orbital phase. The upper plot shows the RV curve of the blue channel, while in the lower one the curve of the red part can be seen. In the bottom of the figures the residuals are illustrated.

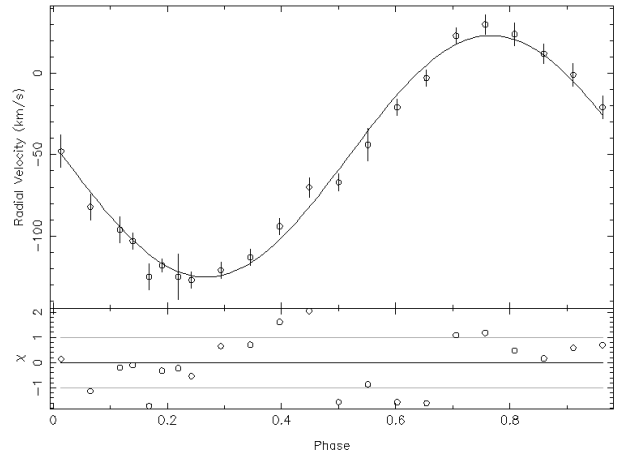

Figure 2. Phased and fitted RV curve of PTF1 J0113 using the Keck ESI spectra. In the bottom panel the residuals are shown.

Table 1. Comparsion of the radial velocities from Palomar DBSP spectra. The second and the third column show the results that we received from the prereduced spectra with the help of SPAS. The fourth and fifth column contain the RVs which we obtained by using the cross correlation. Therefore, we used the spectra that we had reduced with MIDAS.

	old results [km s^{-1}]		new results [km s^{-1}]	
BJD	$v_{\mathrm{rad,blue}}$	$v_{\mathrm{rad,red}}$	$v_{\mathrm{rad,blue}}$	$v_{\mathrm{rad,red}}$
2457015.594689	56 ±8	−24 ±20	12 ±14	-27^{+18}_{-13}
2457015.614567	−41 ±9	−140 ±22	−108 ±7	-136^{+22}_{-21}
2457015.643398	−15 ±9	−96 ±19	-92^{+9}_{-8}	-93^{+18}_{-16}
2457015.661730	82 ±10	−46 ±25	25 ±10	-70^{+22}_{-23}
2457015.664065	59 ±8	−22 ±82	−4 ±12	−76 ±40
2457015.666399	119 ±13	−59 ±35	17 ±14	-53^{+26}_{-27}
2457015.668733	99 ±11	−17 ±48	0 ±15	−37 ±50
2457015.671067	84 ±12	−25 ±56	38 ±13	33^{+40}_{-50}
2457015.673402	114 ±17	−11 ±48	18^{+14}_{-13}	-22^{+29}_{-30}
2457015.675736	161 ±15	−46 ±38	59^{+15}_{-14}	−24 ±29
2457015.678070	123 ±12	−34 ±58	65 ±15	−47 ±40
2457015.680405	115 ±16	−81 ±46	47^{+26}_{-25}	−117 ±40
2457015.682739	120 ±17	−148 ±37	−3 ±14	−127 ±40
2457047.635898	−58 ±13	−121 ±32	-102^{+12}_{-11}	−139 ±40
2457047.638232	−61 ±19	−123 ±23	−114 ±10	-113^{+19}_{-20}
2457047.640566	−55 ±18	−120 ±29	−128 ±11	−114 ±21
2457047.642901	−87 ±9	−153 ±43	−134 ±10	-135^{+26}_{-25}
2457047.645235	−92 ±9	−190 ±32	−160 ±11	-191^{+25}_{-23}
2457047.647569	−106±10	−135 ±35	−138 ±10	-120^{+27}_{-26}
2457047.649903	−92 ±7	−116 ±26	−137 ±10	-123^{+24}_{-25}
2457047.652238	−100±11	−94 ±42	−128 ±12	-89^{+29}_{-28}

problems - circumstances which would require calibration spectra to be taken with the science spectra.

Hence, there was a need to check the data reduction and calibration. First, we validated the position of the telluric lines that can be found only in the red part of the spectra and, therefore, the radial velocities from H_α should be reliable. Nevertheless, we decided to obtain the raw spectra and repeat the data reduction and calibration with another program. The ESO Munich Image Data Analysis System (MIDAS) therefore was used. At the P200 telescope a FeAr-lamp was used for the calibration in the blue and a HeNeAr-lamp in the red. An important preliminary step to the wavelength calibration consists of identifying the emission lines of the recorded calibration spectra which are then used to determine the dispersion relation. This step is necessary because MIDAS needs a few lines (three or more) to be manually identified, before it can associate the other emission lines of the calibration spectra by comparing the identified lines with the line catalogue available in the system. The calibration lines were detected with a simple thresholding algorithm. The identification of the lines was done by a manual comparison of the calibration spectra with the NIST catalogue.

Table 2. Radial velocities from Keck ESI spectra. The last column includes the averaged radial velocity for each spectrum and the corresponding errors (errors calculated by Gaussian error propagation).

MJD	H_α: $v_{\rm rad}$	H_β: $v_{\rm rad}$	H_γ: $v_{\rm rad}$	H_δ: $v_{\rm rad}$	He_{4471} $v_{\rm rad}$	$v_{\rm rad,ges}$ [km s^{-1}]
57578.528575	−107±10	-109±6	−113± 10	−81±10	−105±12	−103±5
57578.533350	−112±12	−128±7	−117±7	−111±10	−124±11	−118±4
57578.538190	−122±10	−139±8	−124±13	−127±11	−124±13	−127±5
57578.542983	−118±13	−130±8	−120±10	−110±12 ±	−130±10	−121±5
57578.547812	−115±16	−128±8	−103±11	-106±12	not used	−113±5
57578.552623	−99±14	−100±9	-90±9	−86±10	not used	−94±5
57578.557427	−56±9	−81±8	−65±10	−77±11	not used	−70±6
57578.562244	−64±12	−66±9	−73±10	−65±10	not used	−67±5
57578.567031	−47±9	−50±9	−34±10	−49±10	−34± 17	−44±10
57578.571842	−20±13	−21±9	−18±8	−21±10	−24±13	−21±5
57578.576617	−7±10	−8±7	−3±11	8±12	not used	−3±5
57578.581428	35±9	40±9	2±10	18±12	not used	23±5
57578.586215	25±18	35 ± 9	39±10	21±13	not used	30±6
57578.591026	39±12	31±9	12±10	13±16	not used	24±7
57578.595813	29±15	17±7	0±10	4±13	not used	12±6
57578.600612	−3±15	3±10	24±16	−34±15	7±22	−1±7
57578.605399	−6±24	−18±11	−37±14	−22±17	−22±12	−21±7
57578.610210	−34±24	−40±13	−74±22	-32±20	not used	−48±10
57578.614997	−80±20	−92±11	−92±17	−65±14	not used	−82±8
57578.619820	−104±19	−100±8	−93±15	−88±12	not used	−96±8
57578.624607	−131±19	−133±13	−124±16	−112±14	not used	−125± 8
57578.629382	−100±39	−115±21	−154±23	−129±23	not used	−125±14

We initially started to examine the FeAr spectra and the calibration of the blue spectra. All emission lines of the FeAr spectra could be identified and the calibration of the spectra of PTF1 J0113 proceeded smoothly. For the calibration of the red channel, the same procedure as for the blue was performed. However, we failed to identify some emission lines of the calibration lamp and could not derive the dispersion relation. For this reason, we had to calibrate individual sections of the spectrum around H_α as well as two telluric bands. The latter were found at the correct wavelengths and we concluded that the H_α radial velocities should be reliable. We used the cross-correlation[3] technique to determine the radial velocity which considers the wavelength-dependency of the Doppler effect. Here, a model spectrum of the same resolution is compared and shifted to the red channel of the sdB spectra until the similarity reaches a maximum. For comparison, the cross-correlation technique was also used for the blue channels of the spectra. We used the data analysis software isis (Interactive Spectral Interpretation System) to carry out the cross-correlation.

Comparison of the radial velocities of the blue parts of the spectra to the red parts revealed that still huge differences between $v_{\rm rad,blue}$ and $v_{\rm rad,red}$ can sometimes occur, but - in contrast to our first approach where the two channels of each spectrum barely matched - the calculated RV values correspond now in the blue and red for at least half of the spectra (see Table 1). There are two possible explanations for this: Firstly, the errors, that were caused by the previous calibration problems, could not be sufficiently corrected or, secondly, the H_α-based RV varies with the orbital phase due to a strong reflection effect filling in the line core as described by Heber et al. (2004). However, we needed better spectra with a higher spectral resolution and a better signal-to-noise (S/N) ratio to resolve this issue.

For this reason, 22 spectra of PTF1 J0113 were recorded with the Keck II 10 m telescope (see section 2). As before, SPAS was used to measure the RVs by fitting a combination of several functions to the absorption lines. Because the covered spectral range was smaller than for the DBSP data, less Balmer hydrogen lines could be used for analysis, namely H_α-H_δ. The results are given in Table 2. The Keck spectra revealed consistent radial velocities derived from each Balmer and the He I 4471 Å line. Hence, the shift, which we saw in the DBSP spectra, is not caused by the reflection effect. The RV curve can be derived, since the system is single-lined and the orbits are circular. A comparison of the best sinusoidal fit curve to the measured radial velocities is shown in Figure 2. The semiamplitute of PTF1 J0113 amounts to K_1=74.2 ± 1.2 km s^{-1}, and the systemic

3 The cross-correlation is defined as the measurement of similarity of two spectra as a function of displacement.

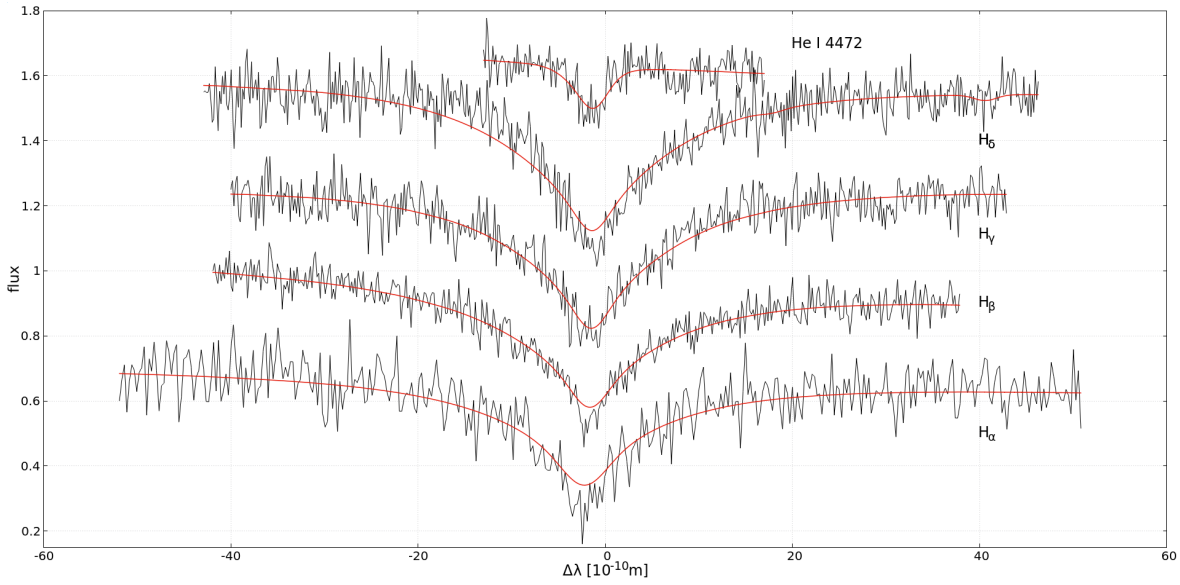

Figure 3. Example fit to several absorption lines of an individual Keck ESI spectrum to determine the atmospheric parameters. The synthetic spectra were calculated from LTE model atmospheres.

velocity is y_1=−51.1 ± 1.7 km s^{-1}. The standard deviation of each parameter is regarded as its 1σ-error. According to Figure 2, the RV curve shows deviations around phase 0.5 that most likely originate from the Rossiter–McLaughlin effect.

3.2 Atmospheric parameters

The atmospheric parameters have been determined by fitting model spectra to the hydrogen Balmer and helium lines, after the single spectra were corrected to zero velocity. Therefore, we used the Keck spectra because they have a higher spectral resolution and a better S/N ratio compared to the DBSP spectra. The model spectra were computed with the help of LTE model atmospheres that were calculated by Heber et al. (2000) with solar metallicity and metal line blanketing. Matching the synthetic hydrogen Balmer lines (H_α - H_δ) and the He I 4471 Å line profiles to the observed spectra (as shown in Figure 3) resulted in the determination of effective temperature $T_{\rm eff}$, helium-to-hydrogen ratio $\log(y) = \log(\frac{n_{\rm He}}{n_{\rm H}})$, and surface gravity $\log(g)$ of each spectrum. First fit attempts showed, that the recorded absorption lines were broader than predicted, which is why we also had to consider rotational broadening. By using SPAS, we could measure the projected rotational velocities of each spectrum using a rotational-line profile as described by Slettebak (1985). The results for the 22 Keck ESI spectra are summarized in Table 3.

Table 3. Atmospheric parameters of PTF1 J0113. Their values were determined with SPAS using the Keck spectra.

$T_{\rm eff}$ [K]	$\log(g)$ $\left[\frac{cm}{s^2}\right]$	$\log(y)$ $\left[\frac{n_{\rm He}}{n_{\rm H}}\right]$	$v_{\rm rot}$ [km s^{-1}]
28256	5.80	−2.29	92 ± 9
28173	5.76	−2.14	74 ± 15
30006	5.68	−2.47	87 ± 17
30422	5.73	−2.22	92 ± 12
29511	5.80	−2.40	73 ± 8
29813	5.81	−2.35	100 ± 17
30171	5.76	−2.44	87 ± 14
30512	5.63	−2.38	72 ± 19
30450	5.79	−2.44	84 ± 11
28710	5.62	−2.41	109 ± 31
29533	5.97	−2.34	80 ± 19
29174	5.80	−2.20	102 ± 17
29196	5.83	−2.14	83 ± 12
28321	5.80	−2.28	88 ± 16
28508	5.85	−2.43	66 ± 16
28918	5.85	−2.24	83 ± 13
28368	5.67	−2.38	58 ± 13
28934	5.77	−2.09	72 ± 14
29480	5.87	−2.49	82 ± 20
29098	5.79	−2.17	90 ± 16
29337	5.89	−2.44	63 ± 20
29292	5.55	−2.28	71 ± 28
Averaged parameters and statistical errors			
29280 ± 720	5.77 ± 0.09	−2.32 ± 0.12	82.8 ± 12.9

Because spectral line profile variations caused by contamination by reflected light from the secondary could be present e.g. as observed for HS 2333+3927 (Heber et al., 2004), we determined the atmospheric parameters for

each orbital phase from every single spectrum. However, in contrast to HS 2333+3927, we did not find any phase dependent variations of the atmospheric parameters to within error limits. Therefore, we adopted the average values of $T_{\rm eff}$=29280 ± 730 K, log(g)=5.77 ± 0.09, and log(y)=−2.32 ± 0.12. The projected rotational velocity was found to be $v \cdot \sin(i)$=82.8 ± 12.9 km s^{-1}.

The atmospheric parameters, which we calculated for every single spectrum, were combined to obtain a higher precision for the derived parameters. These results are consistent with a typical subdwarf B star.

Furthermore, we checked the position of PTF1 J0113 in a $T_{\rm eff}$ – log(g) as well as in a $T_{\rm eff}$-log(y)-diagram and compared this to the currently known HW Vir systems. Its position in the $T_{\rm eff}$ – log(g)-diagram (see Figure 4) is typical for a sdB star. The system's place close to the zero age extreme horizontal branch (ZAEHB) hints at a young post common envelope binary.

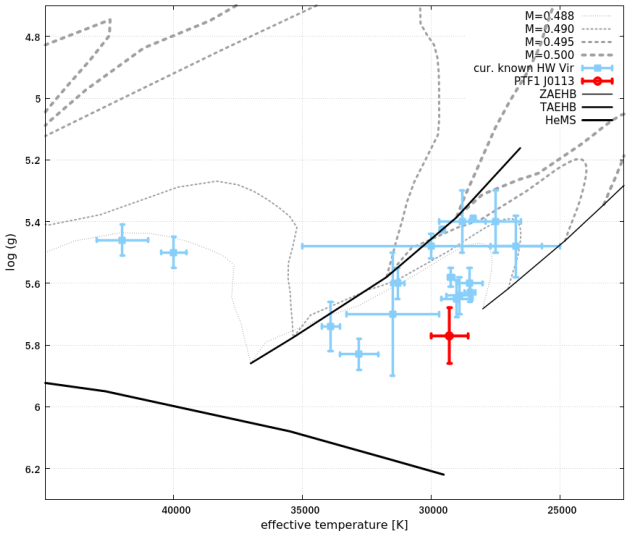

Figure 4. Position of PTF1 J0113 in a $T_{\rm eff}$ – log(g)-diagram. For comparison the other currently known HW Vir systems are shown. Dash dotted lines: Extreme horizontal branch (EHB) evolutionary models for various sdB masses (Dorman et al., 1993). In addition the zero-age extreme horizontal branch (ZAEHB) as well as the terminal age extreme horizontal branch (TAEHB) and the helium main sequence are shown.

In Figure 5, the position of PTF1 J0113 in a $T_{\rm eff}$ – log(y)-diagram is compared to those of the other currently known HW Vir systems. Edelmann et al. (2003) discovered a strong correlation between the helium abundance and the effective temperature of sdBs. They also showed that the sdB stars are separated into two sequences, where the minority (∼ 15%) has a much lower helium abundance compared to the rest. The position of these two groups in

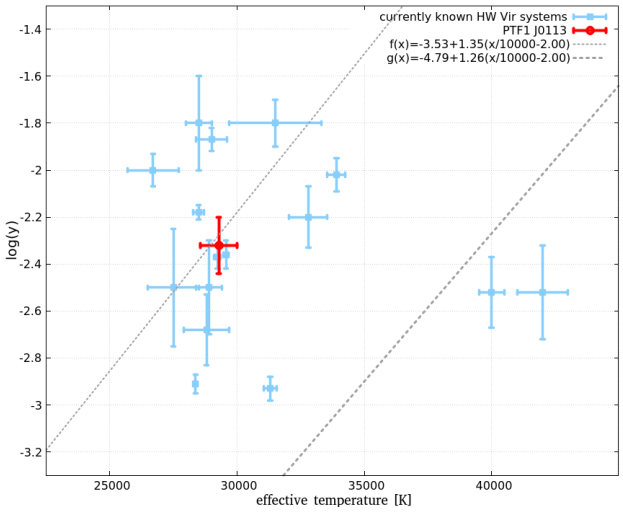

Figure 5. Position of PTF1 J0113 and of the other HW Vir in a $T_{\rm eff}$ – log(y)-diagram. The dash dotted lines describe the relation found for normal helium abundances of sdB stars (Edelmann et al., 2003).

a $T_{\rm eff}$ – log(y)-diagram can be described by means of two linear regression lines, given by $\log(y) = -3.53 + 1.35 \cdot (\frac{T_{\rm eff}}{10^4[K]} - 2.00)$ for the bulk and $\log(y) = -4.79 + 1.26 \cdot (\frac{T_{\rm eff}}{10^4[K]} - 2.00)$ for the minority of sdB stars. Figure 5 demonstrates that sdBs, which are part of a HW Vir system, are showing the same properties as normal sdBs as well as that PTFS11301s is located near the upper regression line. Hence, this system is part of the sdB's majority population.

4 Photometric analysis

The three light curves show prominent reflection effects, with amplitudes around 10% as well as primary and secondary eclipses (see Figure 7).

The reflection effect is caused by a significant difference of the effective temperature of the binary components and bound rotation so that the hemisphere of the cooler star, which is facing the hotter one, is heated up. Across the orbit, we can sometimes see more, sometimes less of the secondary's heated hemisphere. For this reason, the measured intensity of the close binary changes sinusoidally during one period. The primary minimum is very pronounced, the flux descending almost to 50% of the flux at phase 0.25 (see Figure 6).

For further analysis, the light curve was normalized to 1 at phase 0.25. We determined the ephemeris by fitting inverse Gaussians to the primary minimum with the help of gnuplot. As the ULTRACAM light curves only cover one orbital cycle, an accurate determination of the period from this data is not possible. Hence, for the ephemeris, we used

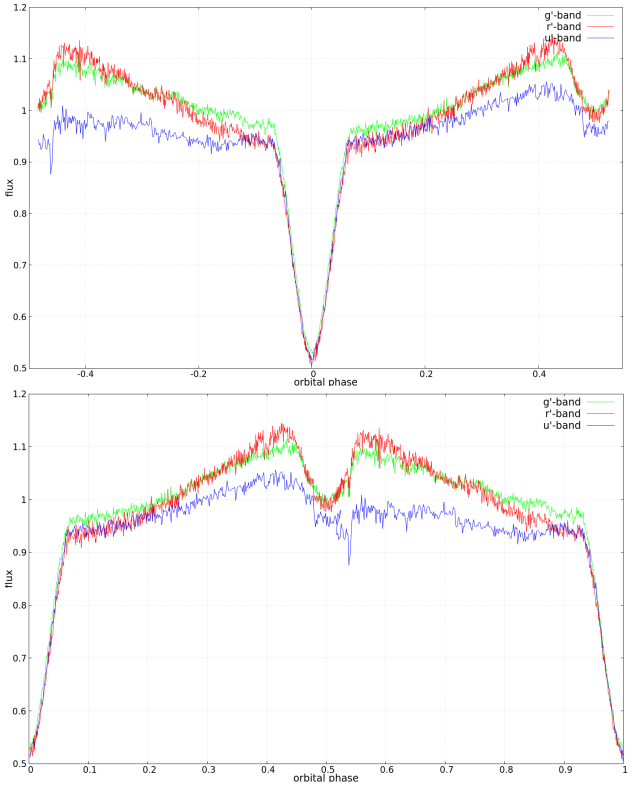

Figure 6. Top: Original ULTRACAM light curves; bottom: Light curves adapted for MORO. The second minimum lays now at $\Phi = 0.5$, the blue light curve is obviously not usable for further analysis.

the PTF light curve that contain two primary minima. We received the period using the Lomb-Scargle periodogram, and with the help of a bootstrapping method, we derived the related error. The ephemeris of the primary minimum was found to be:

$$MJD = 57286.067101(5) + 0.0933731(3) \cdot E,$$

where the error of the primary minimum is the standard error.

For the photometric analysis, we phased and normalized the three ULTRACAM light curves. The light curve analysis was performed using the MOdified ROche program (MORO, see Drechsel et al., 1995) which is based on the Wilson-Devinney code extended by a modified Roche model including radiation pressure effects.

Because MORO needs the light curves to be symmetric around the second minimum at a phase of $\Phi = 0.5$, we had to postpone the left half of each light curve by one orbital phase, as shown in Figure 6. The u'-band light curve could not be used because of an inadequate air mass correction.

Trends are apparent in the g'- and r'-band light curves, but are not corrected. MORO has different modes for various applications. Here, we used the second Wilson-Devinney mode of MORO, which is intended for detached

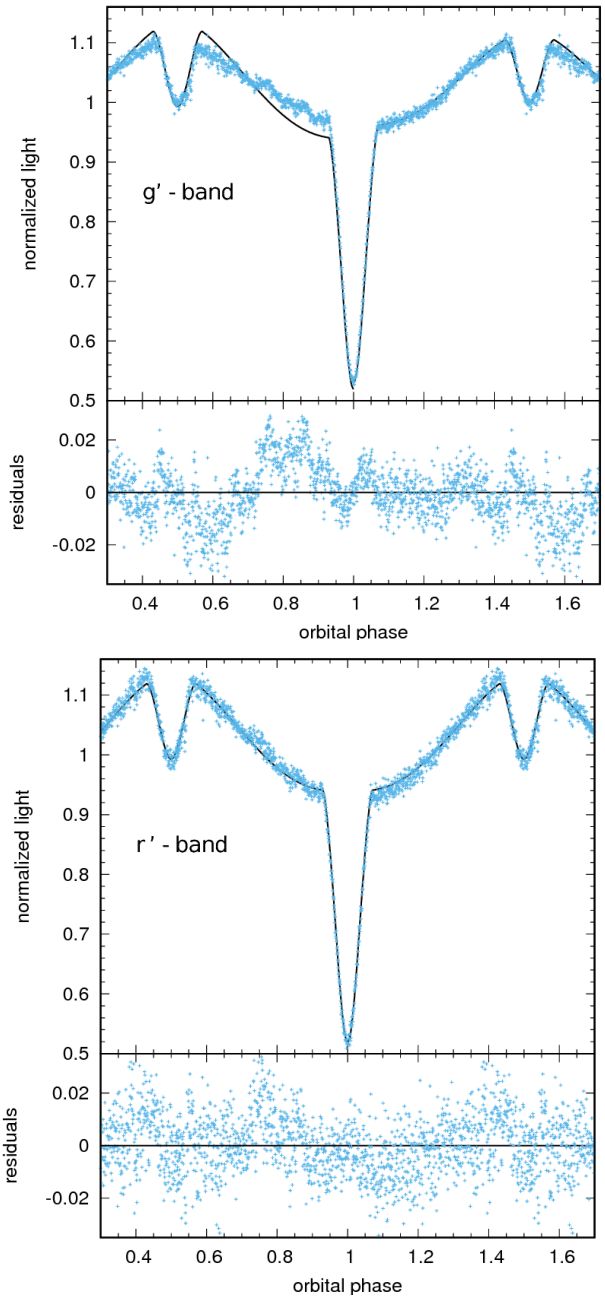

Figure 7. Top: Plot of the fitted green light curve. Left from the primary and right from the secondary minimum: prominent differences between fit and light curve are caused by the atmosphere. Bottom: Plot of the fitted red light curve. The residuals belonging to the plots are shown below each figure.

and semi-detached binaries with a temperature dependent luminosity of the companion. Owing to the high luminosity ratio of the system, where the companion is almost exclusively contributing via a reflection effect, the resulting temperature of the companion is not reliable. The number of free parameters is quite large (12+5N, where N is

the number of used light curves) and constitutes the main problem of light curve analysis, because too many free, partially correlated parameters tend to result in underdetermined solutions. Therefore, some of them had to be fixed making use of the spectroscopic results as well as of theoretical constraints. It is important to note that the mass ratio q - besides the inclination, it is the parameter with the strongest effect to the light curve - strongly correlates with other parameters, such as the Roche potentials Ω or the component radii, and causes a degeneracy of solutions. For this reason, we fixed the mass ratio at preselected values while adjusting the other parameters.

We kept the following parameters fixed: The effective temperature of the primary as well as its surface gravity were taken from the spectroscopic analysis (see Sect. 3.2). The gravity darkening exponent g_1 of the sdB star can be set to 1, as expected for stars with radiative envelopes (von Zeipel, 1924). The secondary is a cool, late type main sequence star with a convective envelope. According to Lucy (1967), its gravity darkening exponent can be fixed at 0.32. Using the tables of Wade & Rucinski (1985), the sdB star's linear limb darkening coefficient was interpolated and set to $x_1 = 0.190$. The radiation pressure of a star depends on its effective temperature and, since late type stars show low temperatures, the radiation pressure effects of the companion are negligible and the related parameter δ_2 of the companion could be set to zero (Drechsel et al., 1995). Furthermore, we found no indication for a third light, which is why we set l_3 to zero. We also fixed the value of bolometric albedo of the sdB at $A_1 = 1$ because every HW Vir system, that was analyzed with MORO, was close to this value (see e.g. Schaffenroth et al., 2014b). All other parameters such as inclination or the Roche potentials were left as free parameters and are listed in Table 4.

We checked a wide range of mass ratios between 0.10 and 0.30, because our first attempts to obtain the RV curve from DBSP spectra proving inconsistent. A lower limit to the mass ratio was found at $q = 0.13$, where the companion fills its Roche lobe. For this reason, we constrained the mass ratio for the detailed analysis to $0.13 < q \leq 0.30$ and calculated for every mass ratio a large grid of synthetic light curves. Both, g' and r' light curve were fitted simultaneously using a classical χ^2 minimization to fit the synthetic light curves to the observations with the help of the simplex algorithm (Kallrath & Linnell, 1987). To estimate the light curves' quality we used the standard deviation of the calculated residuals d_ν:

$$\sigma_{\text{fit}}(x) = \sqrt{\frac{n}{n-m}\frac{1}{\sum_{\nu=1}^{n}\omega_\nu}\sum_{\nu=1}^{n}\omega_\nu d_\nu^2(x)} \qquad (1)$$

Table 4. Best-fit model parameters of the light curve for $q = 0.24$.

Fixed parameters			
Gravity darkening exp.	g_1		1.000
	g_2		0.320
Eff. temp. primary	$T_{\text{eff,prim}}$	[K]	28600
Bolometric albedo	A_1		1.000
Radiation pressure	δ_2		0.000
Luminosity	L_2	[$L_\odot$]	0.0001
Limb darkening coeff.	x_1		0.190
Fraction of third light	l_3		0.000
centr. wavelength	λ_{green}	[mm]	0.4285
	λ_{red}	[mm]	0.6261
Fitted parameters			
Inclination	i	[°]	79.88 ± 0.18
Eff. temp. secondary	$T_{\text{eff,sec}}$	[K]	2705 ± 680
Bolom. albedo	A_2		1.47 ± 0.34
Roche-potential	Ω_1		4.24 ± 0.17
	Ω_2		2.51 ± 0.02
Gravity darkening exp.	δ_1		0.003 ± 0.004
	$L_1(\lambda_1)$	[$L_\odot$]	12.214 ± 0.015
	$L_1(\lambda_2)$		11.927 ± 0.018
Rel. luminosity	$\frac{L_1}{L_1+L_2}$		0.99943 ±0.00032
Limb darkening coeff.	$x_2^d(\lambda_1)$		0.34 ± 0.29
	$x_2^d(\lambda_2)$		0.34 ± 0.29
Roche radii			
	$r_{1,\text{pole}}$	[a]	0.2447 ± 0.0009
	$r_{1,\text{point}}$	[a]	0.2487 ± 0.0009
	$r_{1,\text{side}}$	[a]	0.2470 ± 0.0009
	$r_{1,\text{back}}$	[a]	0.2482 ± 0.0009
	$r_{2,\text{pole}}$	[a]	0.2086 ± 0.0019
	$r_{2,\text{point}}$	[a]	0.229 ± 0.014
	$r_{2,\text{side}}$	[a]	0.2136 ± 0.0021
	$r_{2,\text{back}}$	[a]	0.225 ± 0.005

Notes:
In accordance with Wade & Rucinski (1985)
Test fits: no indication for third light ⇒ parameter set to 0
Central wavelength of the ULTRACAM filters.[4]
L_2 is not independently adjusted, but recomputed from $T_{\text{eff,sec}}$ and r_2. Errors were calculated with the Gaussian error propagation.
In units of the orbital separation

with ω_ν being the weight of each data point ν, m the number of start parameters for the simplex algorithm, and n the number of measurements (Schaffenroth, 2015). The smaller the standard deviation σ_{fit}, the better the fit. Because MORO can not correct residual trends from imperfect air mass correction, we got significant deviations between the observations and the synthetic light curves, especially for phases between $\Phi = -0.3$ and -0.1 as well as to the right side of the second minimum (see Figure 6). For this

4 For more informations visit http://www.vikdhillon.staff.shef.ac.uk/ultracam/

Table 5. Currently known, short-periodic, post common-envelope binaries (PCEBs) which consist of a sdB star and an M-dwarf (dM) or a brown dwarf (BD). Quoted uncertainties are of statistical nature, systematic errors are not included.

System	Period [d]	$T_{\rm eff}$ [K]	$\log(g[\frac{cm}{s^2}])$	$\log(y[\frac{n_{He}}{n_H}])$	references
Currently known HW Vir systems					
NSVS 07826247	0.16177042	29230 ±125	5.58 ±0.03	−2.37 ±0.05	1)
2M1938+4603	0.1257653	29564 ±106	5.425 ±0.009	−2.36 ±0.06	2)
NY Vir	0.101015999	31300 ±250	5.60 ±0.05	−2.93 ±0.05	3)
PTF1 J07245+1253	0.0998025	33900 ±350	5.74 ±0.08	−2.02 ±0.07	4)
HS 0705+6700	0.095646644	28800 ±900	5.40 ±0.10	−2.68 ±0.15	5)
HS 2231+2441	0.110588	28370 ±80.0	5.39 ±0.01	−2.91 ±0.04	6)
HW Vir	0.116719599	28488 ±208	5.63 ±0.03	−2.18 ±0.03	7), 8)
BUL-SC 16335	0.125050278	31500 ±1800	5.70 ±0.20	−1.80 ±0.10	9), 10)
EC 10246-2707	0.118507994	28900 ±500	5.64 ±0.06	−2.50 ±0.20	11)
SDSS J1922+372220	0.168876	27500 ±1000	5.40 ±0.10	−2.50 ±0.25	12)
AA Dor	0.261539736	42000 ±1000	5.46 ±0.05	−2.52 ±0.20	13), 14)
NSVS 14256825	0.11037	40000 ±500	5.50 ±0.05	−2.52 ±0.15	15)
ASAS 10232	0.13927	28500 ±500	5.60 ±0.05	−1.80 ±0.20	16)
SDSS J082053+000843	0.096	26700 ±1000	5.48 ±0.10	−2.00 ±0.07	17)
SDSS J162256+473051	0.0696859	29000 ±600	5.65 ±0.06	−1.87 ±0.05	18)
V2008-1753	0.065817833	32800 ±750	5.83 ±0.05	−2.20 ±0.13	19)
VSX J075328+722424	0.2082535	26200	not av.	not av.	20)
OGLE-GD-ECL-11388	0.147806180	30000 ±5000	5.48 ±0.04	not av.	21)
Konkoly J064029.1+385652.2	0.187284394	55000 ±3000	6.20 ±0.04	−2.24 ±0.40	22)
PTF1 J011339+225739	**0.093348**	**28600±600**	**5.69±0.10**	**-2.21±0.09**	**this work**

References: 1) For et al. (2010), 2) Østensen et al. (2010), 3) Vučković et al. (2007), 4) Schindewolf et al. (2015), 5) Drechsel et al. (2001), 6) Østensen et al. (2007), 7) Lee et al. (2009), 8) Wood & Saffer (1999), 9) Polubek et al. (2007), 10) Geier et al. (2014), 11) Barlow et al. (2013), 12) Schaffenroth (2015), 13) Rauch (2004), 14) Kudritzki et al. (1982), 15) Almeida et al. (2012), 16) Schaffenroth et al. (2013), 17) Geier et al. (2011), 18) Schaffenroth et al. (2014b), 19) Schaffenroth et al. (2015), 20) Pribulla et al. (2013), 21) Hong et al. (2017), 22) Derekas et al. (2015)

reason we double weighted the "better half" of the light curves between $\Phi = 0$ and 0.5, which gave improved values for $\sigma_{\rm fit}$.

Due to the large number of correlated parameters it is not possible to find a unique solution from the light curve alone (Schaffenroth et al., 2013). Hence, we used the spectroscopic results to further constrain the range for the mass ratio. Using the canonical sdB mass and the inclination, which is well constrained by photometry, we got q=0.238 ± 0.006 for the system's mass ratio. For this reason, we adopted $q = 0.24$ to be the best light curve solution. The averaged results for the five best fits at this mass ratio are given in Table 4. The best fitting models together with the data of the ULTRACAM light curves are shown in Figure 7. We find a companion mass of M_{comp}=0.112 ± 0.003 $M_\odot$. The system is seen under an inclination angle of i=79.88 ± 0.18°. While the primary is spherical, its cool companion shows ellipsoidal deformations (see Table 4). Our solution required an albedo of the companion that exceeds 1 ($A_2 = 1.47$) demonstrating that a simple reflection approach fails. The same effect has already been concluded for other HW Vir systems (see Schaffenroth et al., 2013; Schindewolf et al., 2015).

5 Summary

We find that PTF1 J0113 is an eclipsing binary with an orbital period of $P = 0.0933731(3)$d. This system also shows a strong reflection effect at an inclination of nearly 80°. After some problems with the Palomar spectra, we derived a well-defined RV curve with a semi amplitude of K_1=74.2 ± 1.7 km s^{-1} from Keck ESI spectra. A quantitative spectroscopic analysis yielded $T_{\rm eff}$=29280 ± 720 K, $\log(g)$=5.77 ± 0.09, and $\log(y)$=−2.32 ± 0.12, which are typical values for sdB stars, in particular for reflection effect systems (see Table 4). Adopting the canonical mass, we obtained q=0.238 ± 0.006 for the mass ratio by using the mass function, RV curve results, and the canonical sdB mass. With the help of the results of photometry we were able to constrain the mass, radius, and temperature of the secondary to be $M_{\rm comp}$=0.112 ± 0.003 $M_\odot$, $R_{\rm comp}$=0.158 ± 0.009 $R_\odot$, and $T_{\rm eff,comp}$=2705 ± 680 K. The radius of the sdB was found to be $R_{\rm sdB}$=0.178 ± 0.006 $R_\odot$[5]. These results indicate that the companion is a late M-dwarf. Using the canonical mass

5 The errors of the masses and the radii were calculated using the Gaussian error propagation.

and the previously determined radius of the sdB, we can calculate $\log(g)_{phot}$ and compare it to the value of the surface gravity which we derived from spectroscopy. The photometric surface gravity was found to be $\log(g)_{phot}$= 5.61 ± 0.04, and thus the photometric result is a little lower than the one derived from spectroscopy. In summary, our results are showing an eclipsing system that contains a sdB star and an M-dwarf and, hence, this binary is of HW Vir type.

We obtained v_{rot}=82.8 ± 12.9 km s^{-1} for the rotational velocity. Because the binary system is so close, we might expect the sdB's rotation to be tidally locked to the orbit as observed for some other HW Vir stars. However, the star turns out to rotate slightly more slowly than expected for bound rotation (96.8 km s^{-1}). The sdB star might have emerged from the common envelope phase only recently (see Sect. 3.2). Therefore, tidal forces may not have had enough time to spin the sdB up to synchronism.

References

Almeida, L. A., Jablonski, F., Tello, J., & Rodrigues, C. V. **2012**, MNRAS, 423, 478–485

Barlow, B. N., Kilkenny, D., Drechsel, H., Dunlap, B. H., O'Donoghue, D., & Geier, S. **2013**, MNRAS, 430, 22–31

Brown, T. M., Ferguson, H. C., Davidsen, A. F., & Dorman, B. **1997**, ApJ, 482, 685–707

Currie, M. J., Berry, D. S., Jenness, T., Gibb, A. G., Bell, G. S., & Draper, P. W. **2014**, ASPC, 485, 391–395

Derekas, A., Németh, P., Southworth, J., Borkovits, T., Sárneczky, K., Pál, A., & Csák, B. **2015**, ApJ, 808, 179–188

Dhillon, V. S., Marsh, T. R., Stevenson, M. J., Atkinson, D. C., & Kerry, P. **2007**, MNRAS, 378, 825–834

Dorman, B., Rood, R. T., & O'Connell, R. W. **1993**, APJ, 419, 596–614

Drechsel, H., Haas, S., Lorenz, R., & Gayler, S. **1995**, A&A, 294, 723–742

Drechsel, H., Heber, U., Napiwotzki, R., Østensen, R. H., Solheim, J.-E., & Johannessen, F. **2001**, A&A, 379, 893–904

Edelmann, H., Heber, U., Altmann, M., Karl, C., & Lisker, T. **2005**, AAS, 442, 1023–1030

Edelmann, H., Heber, U., Hagen, H.-J., Lemke, M., Dreizler, S., Napiwotzki, R., & Engels, D. **2003**, A&A, 400, 939–

For, B.-Q., Green, E. M., Fontaine, G., Drechsel, H., Shaw, J. S., & Dittmann, J. A. **2010**, APJ, 708, 253–267

Geier, S., Østensen, R. H., Heber, U., Kupfer, T., Maxted, P. F. L., & Barlow, B. N. **2014**, A&A, 562, 95–105

Geier, S., Schaffenroth, V., Drechsel, H., Heber, U., Kupfer, T., Tillich, A., et al. **2011**, ApJ, 731, 22–26

Han, Z., Podsiadlowski, P., Maxted, P., Marsh, T. R., & Ivanova, N. **2002**, PASP, 336, 449–466

Han, Z., Podsiadlowski, P., Maxted, P. F. L., & Marsh, T. R. **2003**, MNRAS, 341, 669–691

Heber, U. **2009**, ARA&A, 47, 211–253

— **2016**, PASP, 128, 966–1051

Heber, U., Drechsel, H., Østensen, R. H., Karl, C., Napiwotzki, R., Altmann, M., & Cordes, O. **2004**, A&A, 420, 251–264

Heber, U., Reid, I. N., & Werner, K. **2000**, A&A, 363, 198–207

Hirsch, H. **2009**, Hot subluminous stars: On the search for chemical signatures of their genesis, PhD thesis, Friedrich-Alexander-Universität Erlangen-Nürnberg

Hong, K., Lee, J. W., Lee, D.-J., Kim, S.-L., Koo, J.-R., Park, J.-H., & Lee, C.-U. **2017**, PASP, 129, 14202–14211

Kallrath, J., & Linnell, A. P. **1987**, ApJ, 313, 346–

Kao, W., Kaplan, D. L., Prince, T. A., Tang, S., Ene, I., Kim, K., et al. **2016**, ApJ, 461, 2747–2761

Kilkenny, D., Hilditch, R., & Penfold, J. **1978**, MNRAS, 183, 523–531

Kudritzki, R. P., Simon, K. P., Lynas-Gray, A. E., Kilkenny, D., & Hill, P. W. **1982**, A&A, 106, 254–260

Law, N. M., Kulkarni, S. R., Dekany, R. G., Ofek, E. O., & Quimby, R. M. **2009**, PASP, 121, 1395–1408

Lee, J. W., Kim, S.-L., Kim, C.-H., Koch, R. H., Lee, C.-U., Kim, H.-I., & Park, J.-H. **2009**, AJ, 137, 3181–3190

Lucy, L. B. **1967**, ZA, 65, 89–92

Marsh, T. R. **1989**, PASP, 101, 1032–1037

Maxted, P. F. L., Heber, U., Marsh, T. R., & North, R. C. **2001**, MNRAS, 326, 1391–1402

Morales-Rueda, L., Maxted, P. F. L., Marsh, T. R., North, R. C., & Heber, U. **2003**, MNRAS, 338, 752–764

Napiwotzki, R. **1999**, A&A, 350, 101–119

Napiwotzki, R., Yungelson, L., Nelemans, G., Marsh, T. R., & Leibundgut, B. **2004**, ASPC, 318, 402–410

Oke, J. B., & Gunn, J. E. **1982**, PASP, 94, 586–

Østensen, R. H., Green, E. M., Bloemen, S., Marsh, T. R., Laird, J. B., & Morris, M. **2010**, MNRAS, 408, 51–55

Østensen, R. H., Oreiro, R., Drechsel, H., Heber, U., Baran, A., & Pigulski, A. **2007**, ASPC, 372, 483–486

Podsiadlowski, P., Han, Z., Lynas-Gray, A. E., & Brown, D. **2008**, ASPC, 392, 15–26

Polubek, G., Pigulski, A., Baran, A., & Udalski, A. **2007**, ASPC, 372, 487–490

Pribulla, T., Dimitrov, D., Kjurkchieva, D., Kohl, S., Kundra, E., Ohlert, J., et al. **2013**, IBVS, 6067, 1–6

Rauch, T. **2004**, Ap&SS, 291, 275–282

Schaffenroth, V. **2015**, Analysis of low-mass and high-mass systems after the common-envelope phase, PhD thesis, Friedrich-Alexander-Universität Erlangen-Nürnberg

Schaffenroth, V., Barlow, B. N., Drechsel, H., & Dunlap, B. H. **2015**, A&A, 576, 123–130

Schaffenroth, V., Classen, L., Nagel, K., Geier, S., Koen, C., Heber, U., & Edelmann, H. **2014**, A&A, 570, 70–75

Schaffenroth, V., Geier, S., Drechsel, H., Heber, U., Wils, P., Østensen, R. H., et al. **2013**, A&A, 553, 18–24

Schaffenroth, V., Geier, S., Heber, U., Kupfer, T., Ziegerer, E., Heuser, C., et al. **2014**, A&A, 564, 98–105

Schindewolf, M., Levitan, D., Heber, U., Drechsel, H., Schaffenroth, V., Kupfer, T., & Prince, T. **2015**, A&A, 580, 117–122

Sheinis, A., Bolte, M., Epps, H., Kibrick, R. I., Miller, J. S., Radovan, M. V., et al. **2002**, PASP, 114, 851–865

Slettebak, A. **1985**, IAUS, 111, 163–183

von Zeipel, H. **1924**, MNRAS, 84, 665–683

Vučković, M., Aerts, C., Østensen, R. H., Nelemans, G., Hu, H., & Jeffery, C. S. **2007**, A&A, 471, 605–615

Wade, R. A., & Rucinski, S. M. **1985**, A&AS, 60, 471–484

Wood, J. H., & Saffer, R. **1999**, MNRAS, 305, 820–828